2014

Iron chaperones PCBP1 and PCBP2 mediate the metallation of the dinuclear iron enzyme deoxyhypusine hydroxylase

Avery Frey
Liver Diseases Branch, National Institute of Diabetes and Digestive and Kidney Diseases, National Institutes of Health

Anjali Nandal
Liver Diseases Branch, National Institute of Diabetes and Digestive and Kidney Diseases, National Institutes of Health

Jong Hwan Park
Oral and Pharyngeal Cancer Branch, National Institute of Dental and Craniofacial Research, National Institutes of Health

Pamela Smith
Liver Diseases Branch, National Institute of Diabetes and Digestive and Kidney Diseases, National Institutes of Health

Toshiki Tabe
Liver Diseases Branch, National Institute of Diabetes and Digestive and Kidney Diseases, National Institutes of Health

See next page for additional authors

Biosensors and Bioelectronics 59 (2014) 112–119

Contents lists available at ScienceDirect

Biosensors and Bioelectronics

journal homepage: www.elsevier.com/locate/bios

Label-free detection of C-reactive protein using a carbon nanofiber based biosensor

Rakesh K. Gupta [a,b], Adaikkappan Periyakaruppan [a,c], M. Meyyappan [a], Jessica E. Koehne [a,*]

[a] NASA Ames Research Center, Moffett Field, CA 94035, USA
[b] Department of Electronics, G. G. M. Science College, Jammu Tawi, 18004, J&K, India
[c] NASA Johnson Space Center, Houston, TX 77058, USA

ARTICLE INFO

Article history:
Received 13 December 2013
Received in revised form
11 March 2014
Accepted 12 March 2014
Available online 26 March 2014

Keywords:
Biosensors
Carbon nanofibers
C-reactive protein
Nanoelectrode array
Electrical impedance spectroscopy etc.

ABSTRACT

We report the sensitive detection of C-reactive protein (CRP), a biomarker for cardiac disease, using a carbon nanofiber based biosensor platform. Vertically aligned carbon nanofibers were grown using plasma enhanced chemical vapor deposition to fabricate nanoelectrode arrays in a 3×3 configuration. Cyclic voltammetry (CV) and electrochemical impedance spectroscopy (EIS) were used for the CRP detection. The CV responses show a 25% reduction in redox current upon the immobilization of anti-CRP on the electrode where as a 30% increase in charge transfer resistance is seen from EIS. Further reduction in redox current and increase in charge transfer resistance result from binding of CRP on anti-CRP immobilized surface, proportional to the concentration of the CRP target. The detection limit of the sensor is found to be ~90 pM or ~11 ng/ml, which is in the clinically relevant range. Control tests using non-specific myoglobin antigen confirmed the specificity of the present approach.

Published by Elsevier B.V.

1. Introduction

Detection and quantification of biomarkers for acute myocardial infraction (AMI) is critical in the diagnosis of cardiovascular diseases. Traditional diagnosis methods for cardiovascular diseases are time consuming and expensive since they are primarily conducted at central clinical laboratories. Faster and inexpensive diagnosis through point-of-care, lab-on-a chip type systems is highly desirable (Mohammed and Desmulliez, 2011). Cardiac troponin (cardiac troponin T (cTnT) and cardiac troponin I (cTnI)), CK-MB (one of the three isoenzyme forms of creatine kinase (CK)) and myoglobin are known as the definitive biomarkers and their elevated concentration in blood remains maintained from few hours to several days upon the occurrence of AMI (Yang and Zhou, 2006). Biomarkers specific to systemic inflammation (SI), a state that occurs much earlier to myocardial necrosis, include C-reactive protein (CRP), myeloperoxidase (MPO), P-selectine etc. and these are known as the biomarkers for earlier detection of acute coronary syndrome (Yang and Zhou, 2006). Among these, CRP, an acute phase protein, is very sensitive and specific to SI, which is synthesized in liver and secreted into blood stream causing infection or inflammation (Du Clos, 2000). The blood plasma concentration of CRP, which increases rapidly several orders during the SI state, can therefore predict future chances of AMI and hence, can help in risk stratification and implementing appropriate and timely therapeutic procedures (Tsai et al., 2007). A rapid and early diagnosis of cardiovascular disease should therefore involve the testing for a definite biomarker (cardiac Troponin, CK-MB or myoglobin) in combination with an early biomarker (C-reactive protein) (Apple et al., 2005).

C-reactive protein has thus become an important candidate for the early detection of cardiovascular events and for setting up preventive measures to reduce the number of deaths due to AMI. There are three different levels of CRP concentrations, suggested by the American Heart Association and the United States Center for Disease control, in human blood serum that evaluates the cardiovascular disease risk: CRP concentration less than 1 μg/ml represents a low risk state, concentration between 1 and 3 μg/ml is considered as average risk and any concentration above 3 μg/ml represents high risk (Bryan et al., 2013; Kushner and Sehgal, 2002). Various studies have proved CRP as a strong predictor of life threatening events such as AMI, giant cell arteritis, arterial disease, stroke and cardiac arrest causing sudden death (Kervinen et al., 2001). Its concentration level in blood rises from a normal level of ≤ 5 μg/ml to > 100 μg/ml in case of systemic infections (Tsai et al., 2007). The reliable means of detection and quantification of CRP concentration thus becomes important for accurate implementation of therapeutic interventions before and after AMI occurrence for monitoring the status of AMI patients. Besides the traditional expensive and time-consuming methods of CRP testing (Roberts et

* Corresponding author.
E-mail address: Jessica.E.Koehne@nasa.gov (J.E. Koehne).

http://dx.doi.org/10.1016/j.bios.2014.03.027
0956-5663/Published by Elsevier B.V.

al., 2000), quantification of CRP using surface plasmon resonance based biosensors (Hu et al., 2006), optical and acoustic biosensors (Luchansky et al., 2011; McBride and Cooper., 2008), enzyme-linked immunosorbent assay (ELISA) (Leung et al., 2005), fluorescence based biosensors (Wolf et al., 2004), magnetic biosensors (Tsai et al., 2007; Martin et al., 2007), electrochemical biosensors based on gold electrode (Bryan et al., 2013; Hennessey et al., 2009), magnetic nano-particles (Tsai et al., 2007) etc., has been demonstrated with a wide range of sensitivity, specificity, cost, turn around time (TAT), immunoassay complexity, flexibility for multiplexing, and detection limit (Qureshi et al., 2012).

Among the available techniques, electrochemical based biosensors have been one of the most successful in offering less expensive, faster, simpler, portable, accurate, flexible for multiplexing and label free detection of a wide range of proteins, nucleic acids, enzymes and other biomolecules. In addition, with the advancements in bioelectronics and biosensors technology using materials such as carbon nanotubes (CNTs) (single and multi-walled) (Jacobs et al., 2010), carbon nanofibers (CNFs) (Li et al., 2012; Vamvakaki et al., 2006) graphene (Kuila et al., 2011), gold nano-wires, nano-structures (Das and Kelley, 2011) and other inorganic wires (Meyyappan and Sunkara, 2010), the sensitivity and detection limits for proteins, nucleic acids etc. have improved tremendously in recent years. Among carbon nanostructures, vertically aligned carbon nanofibers (VACNFs), where each fiber is an individual freestanding nanostructure and acts as a nanoelectrode, have been used successfully to construct biosensors (Li et al., 2005; Cassell et al., 2009; Koehne et al., 2009; Arumugam et al., 2009, 2010; Siddiqui et al., 2010; Periyakaruppan et al., 2011) including detection of cardiac troponin (Periyakaruppan et al., 2013). Due to their small diameter, robustness, high conductivity, biocompatibility and ease of surface modification, VACNF based nanoelectrode arrays (NEAs) serve as a biosensor platform. These VACNFs are typically grown by plasma enhanced chemical vapor deposition (PECVD) wherein the inherent vertical electric field on the substrate platform helps to orient the carbon nanofibers vertically. The VACNFs can be randomly placed on the wafer like a forest or can be precisely positioned at predetermined spots by patterning the growth catalyst on the wafer (Arumugam et al., 2009, 2010; Siddiqui et al., 2010). The nanoelectrode array can be employed with conventional electrochemical techniques such as cyclic voltammetry (CV) (Nicholson, 1965), differential pulse voltammetry (DPV) (Brown and Anson, 1977), and electrochemical impendence spectroscopy (EIS) (Brown and Anson, 1977). Here we use a nanoelectrode array with patterned VACNFs for the detection and quantification of C-reactive protein using both CV and EIS and obtain a detection limit of 90 pM.

2. Materials and methods

2.1. Chemicals and regents

C-reactive protein (2.1 mg protein per ml (lowry)) from human plasma and anti-human C-reactive protein (anti-CRP, 54.7 mg protein per ml (Biuret)) antibody (produced in goat), anti-myoglobin (produced in rabbit, 1:500 protein dilution) as control antibody, myoglobin from human heart ($\geq$ 95%, SDS-PAGE, 2 mg protein per ml (lowry)) as control antigen, 1-ethyl-3-(3-dimethylaminopropyl) carbodiimide (EDC, $\geq$ 99%) and N-hydroxysuccinimide sodium salt (sulfo-NHS, $\geq$ 98% (HPLC)) were purchased from Sigma Aldrich (Saint Louis MO). The stock CRP solution was stored at 4 °C whereas the anti-CRP, anti-myoglobin and myoglobin solutions were stored at −20 °C. Highly pure de-ionized water (18.2 MΩ cm) from super-Q Millipore system was used throughout the study. Phosphate buffered saline (PBS, 10 mM, pH 7.4) was prepared by dissolving PBS sachet (from Sigma Aldrich) in de-ionized water and was filtered using a 0.22 μm membrane filter before every use. Sodium hydroxide (NaOH, 1 mM) solution, for electrochemical etching, was prepared by dissolving appropriate quantity of NaOH pellets (from Sigma Aldrich) in de-ionized water. For continuous use, the anti-CRP solution was stored at 4 °C in working aliquots. Potassium hexacyanoferrate (III) for probe molecule ($Fe[CN_6]^{3-/4-}$) and all other regents used in the study were of analytic grade.

2.2. Nanoelectrode array fabrication using e-beam patterned VACNFs

A 4-inch silicon (100) wafer with 500 nm thermal oxide layer consists of 30 devices (or chips). Each device contains nine identical micro pads (electrodes), each with a surface area of 40,000 μm^2, arranged in 3 × 3 array format as shown in Fig. S1(a) (Supporting Information). Each electrode is interconnected to an individual contact pad (1 mm) for external electrical contact. A brief account of the fabrication procedure is given here. A 200 μm thick chromium (Cr) layer was deposited by e-beam evaporation on optolithographically defined electrodes, contact pads and electrical interconnects. Then the electrodes (micro pads) were spun coated with 400 nm poly(methyl methacrylate) (PMMA) and patterned by using e-beam current (2 nA, 1950 μC/cm^2 at 100 keV). A 10 nm Cr adhesion layer followed by 30 nm nickel catalyst layer were further deposited on these e-beam patterned electrodes. VACNFs were grown from these patterned Ni catalyst particles (Arumugam et al., 2009) using a DC-biased PECVD system (Aixtron, Cambridge, UK). The growth recipe includes acetylene (C_2H_2, 125 sccm) feedstock for carbon source diluted with ammonia (NH_3, 444 sccm) at a pressure of 6.3 mbar, 700 °C and plasma power of 180 W. A 15 min deposition yields ~39,000 free standing VACNFs spaced 1 μm apart on each patterned electrode, where each fiber has a tip diameter of ~80 nm, base diameter of ~100 nm and an average height of ~1.5 μm with Ni catalyst particle on the tip. Passivation of CNF sidewalls and the underlying Cr layer was done by depositing a 3 μm silicon oxide (SiO_2) layer using CVD and employing tetraethylorthosilicate (TEOS) vapor precursor from a liquid source. Planarization of the top electrode surface and exposure of fibers tips were achieved by chemical mechanical polishing (CMP) in two steps, using 0.5 μm alumina (pH 4) for stock removal and 0.1 μm alumina (pH 4) for final polish. Contact pads for electric connection were exposed by optical lithography using a 2.5 μm thick Shipley 3012 resist. Finally the wafer was diced into 30 equal size (~14 mm squares) chips containing nine electrically isolated electrodes (3 × 3 format, 200 μm squares) interconnected with nine contact pads (1 mm squares) for electrical connections. Fig. S1(b) and (c) shows magnified scanning electron microscopy (SEM) (S-4000, Hitachi, USA) images of an individual electrode and VACNF tips embedded in oxide layer. Fig. S1(d) shows an AFM image of the electrode's surface topography with the line section showing the height profile and Fig. S1(e) depicts the 3D schematic of NEA, working electrode along with the exposed fiber tip (Fig. S1(f)).

2.3. Electrochemical characterization

All electrochemical measurements were carried out using a standard three electrodes electrochemical cell connected to a H-CHI660D Instrument, Electrochemical Workstation/Analyzer (CHI Instruments, Inc., Austin, TX). The instrument was interfaced to a personal computer and controlled by associated data processing/analyzing software, chi660d. The electrochemical cell consists of high quality platinum (Pt) wire as counter electrode, saturated calomel electrode (SCE, Accumet, New Hampshire, USA) as reference electrode and nine identical working electrodes of VACNF NEAs connected in a custom designed Teflon liquid cell. The Teflon

liquid cell defines an O-ring of 3 mm diameter and nine connecting pins for electrical contacts to individual working electrodes through contact pads. A 5 mM $K_3[Fe(CN)_6]$ in 1 M KCl electrolyte solution was used to evaluate the electrode characteristics using cyclic voltammetry (CV) and electrochemical impendence spectroscopy (EIS) techniques, before and after modifying the electrode surface with selective probes and target proteins.

2.4. Pre-conditioning of the nanoelectrode array

Before using the e-beam patterned VACNF NEA for bare electrode characteristics or probe/target immobilization, a final polishing step was carried out using non-crystallizing colloidal silica suspension (0.02 μm, from Buehler) on polishing pad (MicroCloth, 73 mm Dia, from Buehler) for 5–7 min, followed by rinsing with isopropyl alcohol (IPA) and de-ionized water and sonication in de-ionized water for 15 min. This final polishing removes the residual debris off the CNF tips, which resulted from the prior CMP procedure. Following sonication, the devices were soaked in nitric acid (HNO_3) for 30 min for two reasons: one is to further clean the CNFs surface and the second is to generate carboxylic acid groups (–COOH) through oxidation on the CNF tips. The devices were then rinsed with de-ionized water and stored in petri dish before use.

2.5. Surface functionalization and probe (anti-CRP) immobilization

Fig. S2(a–c) shows the schematics of electrode surface functionalization and modifications for probes and target bindings. Freshly created carboxylic acid groups on the CNFs tips (Fig. S2 (a)) were used for probe (anti-CRP) immobilization using carbodiimide crosslinking. Prior to probe immobilization and in order for stable terminal activation of carboxylic acid groups, a reaction of coupling regents (linker) solution containing 0.4 M EDC and 0.1 M sulfo-NHS in PBS (10 mM, pH 7.4 and 1:1 volume) was carried out with VACNFs for 30 min. The functionalized devices (with linker molecules) were then rinsed gently with PBS twice for 10 min to remove unstable (loosely attached) linker molecules off the electrodes surface and the devices were later allowed to dry at room temperature. Following the linker functionalization, 50 μL of anti-CRP (20 μM) solution in PBS (10 mM, ph 7.4) was spotted to the VACNFs in the electrode and incubated at room temperature for one hour. The reaction between the primary amine groups in anti-CRP and –COOH groups at the VACNF tips resulted in the formation of stable amide bonds between anti-CRP and VACNFs as shown in Fig. S2(b). Loosely-bonded anti-CRP and other non-specific bindings were eliminated from the electrode surface by stringent rinsing for 15 min in three steps; twice with PBS (2×5 min) and once with de-ionized water (5 min) while shaking the device at room temperature. Prior to electrochemistry readout, rinsing with de-ionized water was necessary to remove PBS from the electrode surface with anti-CRP immobilized on VACNF tips. After the electrochemical readout, the devices were rinsed gently with de-ionized water and allowed to dry before incubating specific concentration of CRP on anti-CRP immobilized electrode surface.

2.6. CRP binding to immobilized anti-CRP probes

For evaluating the limit of detection (LOD) of the sensors, different concentrations (from 50 ng/ml to 5 μg/ml) of CRP were prepared by adding specific quantity of CRP from the stock concentration (2.1 mg/ml) in different amounts of PBS (10 mM, pH 7.4). A known concentration of CRP was allowed to react and covalently bind with anti-CRP probes for 1 h by dropping the CRP solution on the device. The schematic shown in Fig. S2 (c) represents the specific CRP binding with anti-CRP. Non-specifically attached molecules (by-products) were removed by stringent rinsing of the device for 15 min in three steps: twice with PBS (2×5 min) and once with de-ionized water (5 min) whilst shaking the device at room temperature. The devices were allowed to dry before taking the electrochemical readout.

2.7. Detection and quantification of target CRP

Electrochemical techniques (CV and EIS) were employed for qualitative as well as quantitative detection of CRP. CV and EIS data characterizing bare working electrodes and subsequent VACNF surface modifications (Linker\anti-CRP\CRP) were acquired using the addition of $([Fe(CN)_6]^{-3/-4})$ in the potential region of its reduction and oxidation. CV data sets were recorded in the potential window from −400 mV to 800 mV vs. SCE at 20 mV/s. EIS data of the same working electrodes were collected across a frequency range of 0.1 Hz to 100 KHz while applying a 10 mV sine wave with the direct current potential set to 0.175 mV (standard potential of 5 mM $K_3[Fe(CN)_6]$ in 1 M KCl). CV curves (for bare and different surface formations) were plotted using chi660d software for qualitative detection of CRP. EIS data was plotted in the complex plane diagrams (Nyquist plots) and fitted through ideal Randle's equivalent circuit. CRP presence at anti-CRP-modified VACNF electrodes was detected by investigating the changes in reduction current in CV plots and charge transfer resistance (R_{ct}) in EIS plots. The decrease in the electrode effective area with the subsequent surface modifications (i.e. coverage of effective area with anti-CRP and CRP) results in substantial increase in "R_{ct}". The increase of "R_{ct}" after CRP binding on anti-CRP immobilized electrode surface (decrease in effective surface area) indicates the detection of CRP. The "R_{ct}" over the specified range of CRP concentrations was recorded and analyzed for quantification and determination of LOD. The average values of "R_{ct}", recorded from 3–5 electrodes immobilized with specific concentration of anti-CRP for different CRP concentrations (from 50 ng/ml to 5 μg/ml) were plotted using excel software. The error bars represent the standard deviation of collected data. The electrochemical curves (CV and EIS) for bare and subsequent surface modifications with anti-CRP and CRP were plotted using chi660. The LOD was calculated from the response equivalent to three times the noise signal or zero target response (anti-CRP).

2.8. Detection of non-specific control protein

To verify the specificity of CRP immunoassay, CV and EIS data were collected with identical conditions and parameters as described earlier for the evaluation of non-specific control proteins binding on the device. Two such assays were investigated, one with myoglobin as antigen for anti-CRP antibody immobilized device and second with CRP as antigen for anti-myoglobin antibody immobilized device. The incubation and sensing methods were the same as employed for specific antigen–antibody immobilization, as described earlier but with high concentrations used for both types of antigen proteins CRP (2 mg/ml) and myoglobin (2 mg/ml).

3. Results and discussion

3.1. Electrochemical evaluation of the VACNF NEA sensor

Prior to the surface modifications (immobilizing probes and targets) of the VACNF NEA, electrochemical characterization of unmodified or bare electrodes was done utilizing 5 mM $K_3[Fe(CN)_6]$ in 1 M KCl to evaluate electrode quality. SEM images of the individual electrodes were first inspected for exposed fibers tips in

order to facilitate the electrochemical evaluation and surface functionalization for probe–target proteins bindings; Fig. S1(c) is a SEM image of one of the working electrodes in the 3×3 array device. The VACNFs tips are the bright dots embedded in SiO_2 layer (shaded). AFM micrograph (Fig. S1(d)) of the same electrode confirms the fiber diameter to be ~80 nm when estimated at half-width points on the height profile line section. The combination of reactive ion etching (RIE) and CMP employed for surface planarization results in protruded VACNF tips around 30–50 nm above the oxide surface. These projections of VACNF tips above the surface are primarily due to the resilient nature of the fibers (Li et al., 2005). The iron ions ($Fe[(CN)_6]^{3-/4-}$) present in the electrolyte solution probe the working electrode surface while exchanging the electrons with exposed VACNF tips. The exchange of electrons between the redox ions ($Fe[(CN)_6]^{3-/4-}$) and VACNFs causes the redox reaction given below

$$Fe[(CN)_6]^{3-} + e^- \leftrightarrow Fe[(CN)_6]^{4-} \quad (1)$$

The resulting redox current is proportional to the electrode surface area. Therefore, electrode surface modifications with anti-CRP probes and CRP targets would block the redox current, thus providing the means of detection of CRP antigens on anti-CRP immobilized electrode surface as mentioned earlier. Following the pre-conditioning of VACNF NEA device as outlined earlier, CV and EIS measurements for bare and modified electrodes were carried out. Fig. 1(a) shows the typical steady state sigmoidal behavior of an individual electrode whereas Fig. S3(a) under Supplementary Information provides CV curves for three different electrodes (E1–E3) showing the steady state peaks at a potential difference of ~400 mV (Cassell et al., 2009; Koehne et al., 2009; Arumugam et al., 2009, 2010; Siddiqui et al., 2010). The steady state behavior is expected from a spatially patterned isolated nanofiber electrode because of the absence of overlapping diffusion layers and predominant radial diffusion of solution ions ($Fe[(CN)_6]^{3-/4-}$) towards the nanoelectrodes.

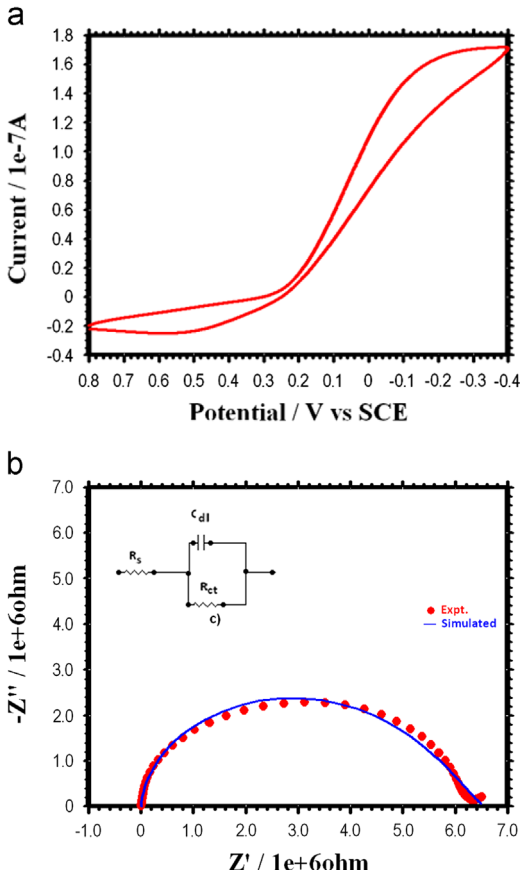

Fig. 1. Electrochemical characterization of VACNF electrode recorded in electrolyte solution containing 5 mM $Fe[CN_6]^{3-/4-}$ in 1 M KCl. (a) CV and (b) EIS; dotted curve represents the measured data and solid line shows the simulated data using ideal Randle's circuit (inset).

The CV curves in Fig. 1(a) and Fig. S3(a) show slower electrode kinetics ($\Delta E_p \sim 400$ mV), which, however, can be improved by electrochemical activation of VACNFs on individual electrodes. Electrochemical etching in 1.0 M NaOH at 1.2 V for 30 s followed by soaking in 1 M HNO_3 for 15 min would improve the electrode kinetics ($\Delta E_p \sim 100$ mV) and reduction currents while opening the edge planes of the fibers as reported by Lim et al. (2004). We observed (data not shown) that even few seconds of electrochemical etching of VACNFs results in substantial etching of the fiber tips causing them to recess into the oxide surface, thereby leaving holes (shallow VACNFs) on the electrode surface (Siddiqui et al., 2010; Arumugam et al., 2010). This geometry is not ideal for antibody immobilization and electrochemical etching therefore was avoided; however 30 min HNO_3 acid soaking was done in order to improve the signal strength. The effective VACNF density (number of active fibers) on an individual electrode can be calculated from the steady-state CV current using the relation, $I_{ss} = 4NnFDCr$ (Lim et al., 2004; Bard and Faulkner, 2001), where 'N' is the number of exposed fibers on the electrode (micro pad), 'n' is the number of electrons exchanged per molecule, 'F' is the Faraday constant, 'D' (cm^2/s) is the diffusion coefficient of redox species, 'C' ($mole/cm^3$) is the bulk concentration of redox species and 'r' is the average radius of VACNFs. Therefore, for $I_{ss} = 180$ nA, $D = 6.3 \times 10^3$ cm^2/s, $C = 5$ mM, and $r = 40$ nm, the effective number of VACNFs on the electrode is ~1850, which is consistent with results reported earlier (Arumugam et al., 2009, 2010; Siddiqui et al., 2010). A higher value of 'I_{ss}' implies higher number of VACNFs active on the patterned electrode and in addition to this, a small background current (due to non-overlapping radial diffusion) provides higher detection sensitivity and signal to noise (S/N) ratio of the electrode. We, however, observed variations in the effective VACNF density from electrode-to-electrode as well as device-to-device, which can be easily calculated from the known values of steady state currents as discussed above. Variations in the effective VACNF density can be attributed to CNFs of unequal lengths and/or failure of some catalyst particles to initiate fiber growth. The effective density of VACNFs and their activation would eventually result in variations in probe–target protein bindings and hence, device sensitivity and limit of detection.

Fig. 1(b) shows the impedance spectrum (EIS) for the same unmodified or bare electrode whereas Fig. S3(b) in the Supplementary Information shows the EIS of three electrodes (E1–E3). The EIS technique provides better sensitivity than CV by measuring the charge transfer resistance of exposed VANCFs interfaced with the solution (Hennessey et al., 2009). The complex plane (Nyquits plots) representation of impedance values in Fig. 1(b) is recorded which describes a time constant component representing charge transfer resistance (semicircle) over the frequency range of 0.1 Hz to 100 KHz and a very small characteristic linear response representing the mass transport process (Warburg impedance). The intersection of the semicircle on the horizontal axis (real impedance) gives the charge transfer resistance (R_{ct}) value of the specific electrode. We observe a very small or no Warburg impedance (W) in some cases, which is expected because of the absence of overlapping diffusion layers in spatially patterned VACNF NEA (Siddiqui et al., 2010). A small but apparent contribution of 'W' in impedance spectrum at lower frequency can be attributed to mass transport caused by the accumulation of redox reaction products (oxidized and reduced species) around the fiber tips. For quantitative values of R_{ct}, the EIS spectrum of the individual electrode can be modeled using an ideal Randle's

equivalent circuit (REC, inset in Fig. 1(b)) comprising of solution resistance component 'R_s (Ω)' in series with time constant element comprising of charge transfer resistance component 'R_{ct} (Ω)' and double layer capacitance $C_{DL}(F)$ component of REC. A better agreement between experimental and simulated curves can be obtained by using frequency-dependent constant-phase-elements (CPE) replacing pure 'C_{DL}' with 'CPE_{DL}' and in addition 'CPE_w' in series with 'R_{ct}' as suggested by Hennessey et al. (2009). However, the 'R_{ct}' can easily be quantified from the predictable intersection of semicircle (experimental curve) on the horizontal axis (real impedance) in the EIS plot. For three different electrodes (E1–E3), the CV curves (Fig. S3(a)) and impedance curves (Fig. S3 (b)) apparently follow Ohm's law qualitatively, as the 'R_{ct}' values increase ($R_{ct(E3)} > R_{ct(E2)} > R_{ct(E1)}$) with a decrease in the slope and 'I_{ss}' of the reduction current (negative potential scan) ($I_{ss(E1)} > I_{ss(E2)} > I_{ss(E3)}$). The higher sensitivity of the EIS technique can be seen compared to CV in terms of sharp changes in 'R_{ct}', than the respective changes in slope or 'I_{ss}'.

Binding of specific amount of CRP with surface immobilized anti-CRP on the VACNFs would block the diffusion of Fe $[(CN)_6]^{3-/4-}$ towards the electrode surface. It is, therefore, anticipated that the subsequent modifications of VACNFs with anti-CRP antibody and specific concentrations of CRP antigen would block the charge transfer process between Fe $[(CN)_6]^{3-/4-}$ and VACNFs resulting in the respective decrease of steady state redox current 'I_{ss}' or increase in the 'R_{ct}', thus enabling detection of the specific CRP concentration.

3.2. Electrochemical detection of C-reactive protein

CRP detection using fluorescence techniques and labeled functional magnetic nanoparticles based immunoassay has been developed with high sensitivity, selectivity and lower LOD (Tsai et al., 2007; Wolf et al., 2004). These immunoassays, however, involve either CRP protein labeling or additional complex sensing surface modifications for selective capture of CRP under magnetic fields, in addition to increasing the cost and time of assay. In contrast, we employ a label-free and facile detection strategy, where the binding of specific CRP target protein with surface immobilized anti-CRP capture protein is investigated by redox molecule ($Fe[(CN)_6]^{3-/4-}$) using well established electrochemical approaches. A wide range of CRP concentrations, from 50 ng/ml to 5 μg/ml (equivalent to 420 pM to 42 nM) was investigated in order to evaluate the sensitivity and detection limit of the sensors. The electrochemical responses of anti-CRP modified electrodes was considered as the baseline or zero target response and the corresponding variations in 'I_{ss}' and 'R_{ct}' with respect to the surface concentration of CRP was recorded using CV and EIS for CRP quantification.

Fig. 2(a) shows CV curves recorded for the bare electrode, Linker\anti-CRP probes and Linker\anti-CRP\CRP target proteins. The bare electrode response shows a sigmoidal response with steady state peaks and potential separation (ΔE) of 400 mV. This peak potential, however, can be reduced to 100 mV by electrochemical etching, which has been avoided here to avoid the possibility of non-specific adsorption in the recessed VACNFs sites as discussed earlier. Cathodic steady state occurs in the negative potential range of the CV scan, where the reduction of iron molecules at the surface of the working electrode takes place converting the reactants ($Fe[(CN)_6]^{3-}$) to products ($Fe[(CN)_6]^{4-}$) while accepting an electron per iron molecule from electrode. In contrast, anodic steady state occurs in the positive potential range of the CV scan due to back conversion of $Fe[(CN)_6]^{4-}$ to $Fe[(CN)_6]^{3-}$ while donating an electron per iron molecule to the working electrode. In this process, the reverse current encounters the double layer capacitance (due to $Fe[(CN)_6]^{4-}$ accumulation

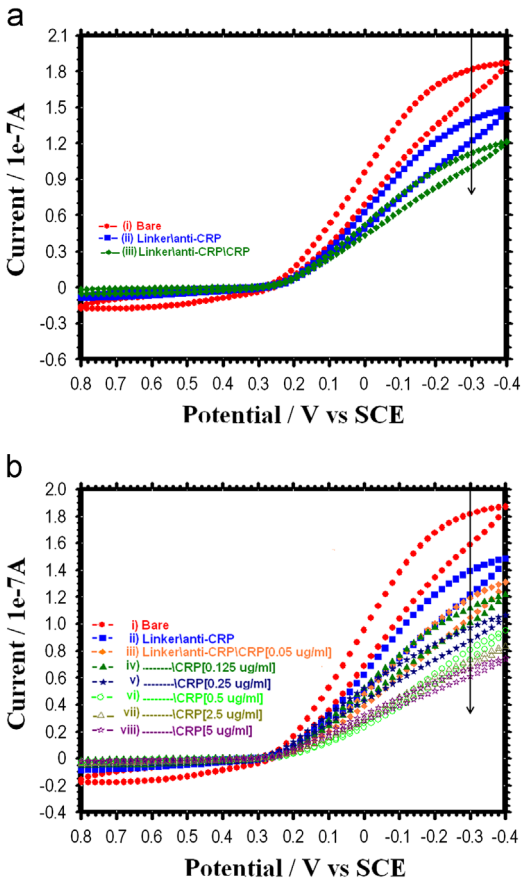

Fig. 2. Selected CV curves for bare and subsequent modified electrodes recorded in electrolyte solution containing 5 mM $Fe[CN_6]^{3-/4-}$ in 1 M KCl; (a) CV; bare (i), Linker\anti-CRP (ii), Linker\anti-CRP\CRP and (b) bare (i), Linker\anti-CRP (ii), Linker\anti-CRP\CRP [0.05–5 μg/ml](iii–viii).

near the electrode), resulting in a slower current response. The forward and reverse CV scans thus give a qualitative measurement of the surface capacitance, which is proportional to the width of the double layer. In the case of patterned VACNF NEAs, each fiber tip is ~1 μm apart from its neighbor which minimizes overlapping of the double layers from neighboring electrodes, thus yielding a sigmoidal CV wave in comparison to reversible CV with well defined redox peeks seen in the case of macro-electrodes (high density randomly grown VACNFs) in which diffusion layer overlapping is most prevalent (Periyakaruppan et al., 2013).

The presence of anti-CRP on the VACNF tips (Fig. S2(b)) would physically insulate the electrode's active surface area. This insulating layer would reduce the amount of charged species ($Fe[(CN)_6]^{3-/4-}$) diffusing towards the electrode which, in turn, would reduce the amount of electrons exchanged with the VACNFs and thus, a decrease in the redox currents i.e. flattening of the CV curve has been recorded for electrodes immobilized with anti-CRP. The CV response of Linker\anti-CRP (curve (ii)) in Fig. 2 (a) demonstrates a substantial decrease in current compared to that of bare electrode, which clearly indicates the presence of anti-CRP. The percentage decrease in the anti-CRP current with respect to that of the bare electrode can be estimated by calculating the ratio of two cathodic (reduction) currents on in Fig. 2(a) at constant potential by using Eq. (2)given below:

$$\Delta I(\%) = \left|1 - \left[\frac{I_{anti-CRP}}{I_{bare}}\right]_{E=const}\right| \times 100 \quad (2)$$

where 'ΔI' represents the change in current, '$I_{anti\text{-}CRP}$' and 'I_{bare}' represent the reduction currents for anti-CRP immobilized and

bare electrode respectively. This percentage decrease in anti-CRP current gives a measure of the apparent surface coverage of the electrode by anti-CRP. A 25% decrease in anti-CRP current was estimated at 300 mV potential. A further decrease in redox current is seen when CRP binds with anti-CRP immobilized on the electrode due to further insulation of the active surface area of the working electrode. A measure of the decrease in CRP reduction current ('I_{CRP}') with respect to '$I_{anti\text{-}CRP}$' at −300 mV can indicate the detection of the specific concentration of CRP bound on anti-CRP immobilized sensor surface. Fig. 2(b) shows CV curves for bare, Linker\anti-CRP and different CRP concentrations studied here. The respective decrease in 'I_{CRP}' at −300 mV with varying concentrations is due to the relative coverage of the electrode surface with CRP. The currents decrease at faster rates for lower CRP concentrations (0.05–0.5 μg/ml) and at slower rate for higher concentrations (2.5–5 μg/ml), which is consistent with previous studies (Li et al., 2005). In addition to the decrease in current values, a decrease in the surface capacitance with increase in CRP concentration is also seen from the closeness of the forward and reverse CV scans. This decrease in surface capacitance results from the smaller accumulation of $Fe[(CN)_6]^{4-}$ molecules near the VACNF tips, as discussed earlier.

EIS was also used to investigate the interaction of anti-CRP and CRP with the electrode surface through the 'R_{ct}' of the working electrode to monitor the electron transfer kinetics. Fig. 3(a) shows the EIS curves recorded for the bare, Linker\anti-CRP and Linker \anti-CRP\CRP target protein layers on the electrode. Predictably, the 'R_{ct}' values increase from ~7 MΩ for the bare electrode to ~10 MΩ for Linker\anti-CRP and further with the binding of

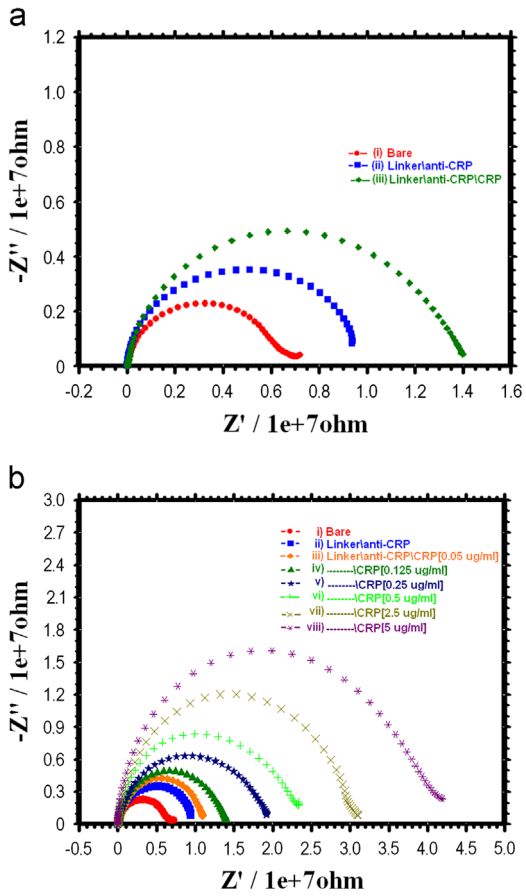

Fig. 3. Selected EIS curves for bare and subsequent modified electrodes recorded in electrolyte solution containing 5 mM $Fe[CN_6]^{3-/4-}$ in 1 M KCl; (a) bare (i), Linker \anti-CRP (ii), linker\anti-CRP\CRP and (b) bare (i), Linker\anti-CRP (ii), Linker\anti-CRP\CRP [0.05–5 μg/ml](iii–viii).

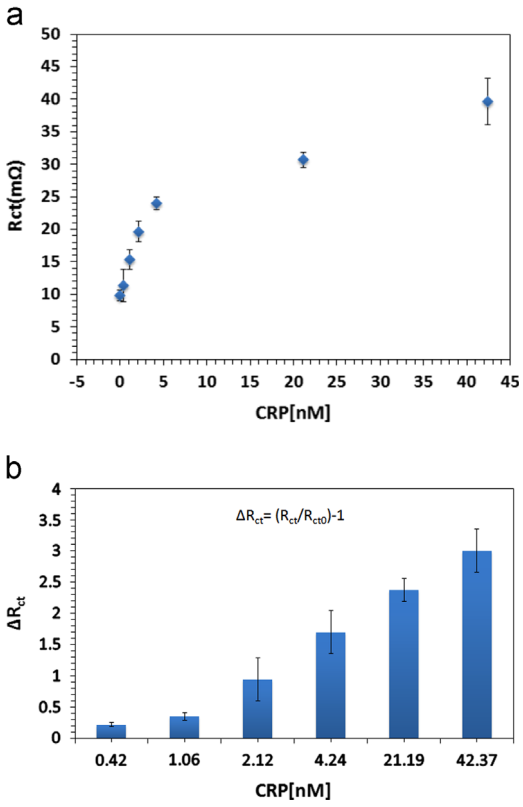

Fig. 4. Recorded 'R_{ct}' values and respective change in charge transfer resistance 'ΔR_{ct}'; (a) 'R_{ct}' vs. different concentrations of CRP on anti-CRP immobilized device, (b) change in 'R_{ct0}' (charge transfer resistance for anti-CRP) with respect to different CRP concentrations.

specific concentrations of CRP with anti-CRP. The percentage change in 'R_{ct}' for anti-CRP from bare electrode resistance is calculated as:

$$\Delta R_{ct} = \left[\frac{R_{ct_{anti-CRP}}}{R_{ct_{bare}}}\right] - 1 \quad (3)$$

where '$R_{ct_{anti-CRP}}$' denotes the resistance for anti-CRP immobilized and '$R_{ct_{bare}}$' is the resistance for bare electrode. A ~30% increase in 'R_{ct}' for electrode immobilized with anti-CRP is estimated, which is close to the 25% change in current from the corresponding CV analysis discussed earlier. This considerable increase in 'R_{ct}', with the subsequent coverage of the electrode surface (with anti-CRP and further with specific concentration of CRP), is consistent with the blockage of redox species reaching to the electrode for charge exchange. Also, the currents measured in CV and the resistances measured in EIS are inversely proportional to each other, qualitatively obeying the Ohm's law. A distinctly measurable increase in 'R_{ct}' values after the surface modifications also indicates the high sensitivity of EIS compared to the CV technique, as reported by Hennessey et al. (2009). Fig. 3(b) presents EIS curves for bare, Linker\anti-CRP and different CRP concentrations studied here. An increase in 'R_{ct}' is seen, as expected, with CRP concentration. Fig. 4 (a) plots the average values of 'R_{ct}' for different CRP concentrations (from 0 to 42 nM); normalization of EIS data as shown in Eq. (4) is necessary here to incorporate the variations in initial charge transfer resistance (pad-to-pad and device-to-device variation) due to the factors discussed in Section 3.1.

$$\Delta R_{ct} = \frac{R_{ct}}{R_{ct0}} - 1 \quad (4)$$

where 'R_{ct0}' depicts the charge transfer resistance for anti-CRP modified (Linker\anti-CRP) electrode. In Fig. 4(b) depicting the

normalized values (ΔR_{ct}) for each CRP concentration, two slopes are seen with respect to CRP concentrations. The smaller slope is observed in the region of lower CRP concentrations (0.42 and 1.06 nM) where the respective % increase in 'R_{ct}' is small (~13% per decade of change in CRP concentration). As the CRP concentration rises above 1.06 mM (0.125 μg/ml), 'R_{ct}' increases sharply (~60% per decade of change in CRP concentration).

The detection of CRP here shows an LOD (limit of detection) of ~90 pM (equivalent to ~11 ng/ml), which is calculated by extrapolating the assay's linear range in the lower concentration region and looking for a response equivalent to three times the standard deviation of zero target response (data not shown). The estimated low detection limit, slightly better than the recently reported 176 pM limit (Bryan et al., 2013), provides sufficient sensitivity for clinical practice or for point of care testing. The patterned VACNF NEA is ultrasensitive with small LOD and high S/N ratio because of its small double layer capacitance around the VACNF tips, absence of overlapping of diffusion layers from individual neighboring fibers, and radial instead of linear flow of charged species from the electrolyte solution towards the nano-sized electrodes. Higher sensitivity and lower LOD are possible through smaller R_{ct0}, which indeed requires smaller initial electrode resistance ($R_{ct_{bare}}$). The lower ($R_{ct_{bare}}$) can be achieved by VACNF activation (i.e. faster electrode kinetics) while keeping the electrode surface area (VACNFs density) constant. Achieving this while preventing recessed CNFs mentioned earlier requires optimization of the current approach or seeking new routes, which is currently under way.

3.3. Specificity test: control protein detection

To confirm the specificity of developed CRP assay, the sensor was evaluated with non-specific myoglobin antigen. Fig. 5 (a) shows CV curves for bare, Linker\anti-CRP layer and Linker\anti-CRP\myoglobin layer electrode. It is evident that there is no non-specific (myoglobin) binding with anti-CRP. However, an increase in the electrode current (curve (iii)) indicates the possibility of further electrode cleaning and removal of loosely or unstable bonded anti-CRP off the electrode surface due to the excessive rinsing after the myoglobin protein incubation. Absence of non-specific target binding with anti-CRP antibody has been further confirmed by EIS data in Fig. 5(b). A decrease in the 'R_{ct}' after myoglobin incubation on anti-CRP layer is consistent with CV data. Fig. 5(c), insets in Fig. 5(b), show the average values of 'R_{ct}' for bare and subsequently modified electrodes with probe antibodies (anti-CRP) and non-specific target antigens (myoglobin). On average, a ~12% reduction in 'R_{ct}' after non-specific target protein binding has been estimated. A similar set of CV and EIS experiments was carried out after incubating CRP as target protein on anti-myoglobin immobilized electrode. A similar result with a ~13% (data not shown) reduction in 'R_{ct}' after CRP incubation on anti-myoglobin immobilized electrodes was observed.

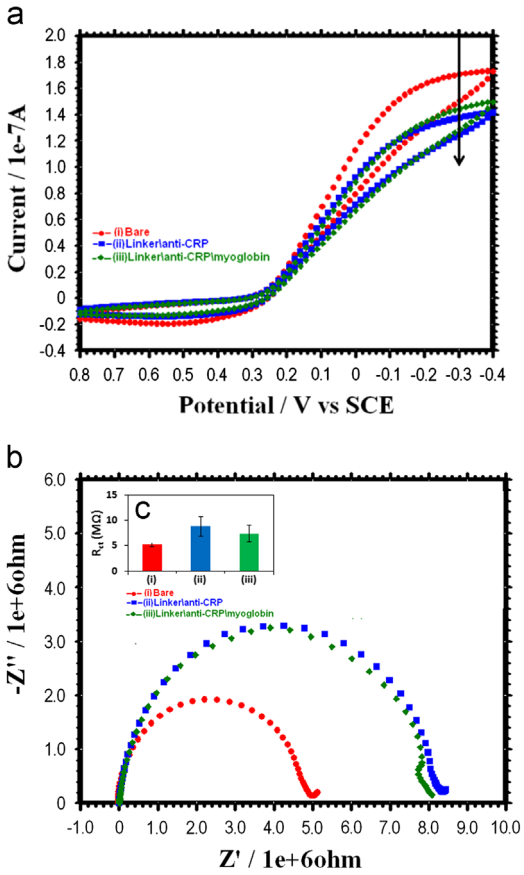

Fig. 5. Control test recorded in electrolyte solution containing 5 mM $Fe[CN_6]^{3-/4-}$ in 1 M KCl. (a) CV and (b) EIS for (i) bare, (ii) Linker\anti-CRP and (iii) Linker\anti-CRP\myoglobin. (c) Average values of 'R_{ct}' for (i) bare, (ii) Linker\anti-CRP and (iii) Linker\anti-CRP\myoglobin.

4. Conclusion

A highly selective, facile, low cost and label-free electrochemical sensing using a nanoelectrode array with patterned vertically aligned carbon nanofibers has been developed for the detection of CRP, a biomarker for early stage acute myocardial infraction. The impedance spectroscopy results show that the approach is capable of detecting CRP down to ~90 pM or ~11 ng/ml, a clinically relevant range, with sufficient sensitivity. The non-specific protein (myoglobin) binding data confirm the high selectivity of the developed assay. Integration of the nanoelectrode array with micro-fluidics capability can provide a portable and multiple protein detection platform, as desired in diagnosis and for point-of-care systems. Reducing the initial resistance of the electrodes can further reduce the LOD, which is currently being investigated. It is critical to evaluate the sensitivity, detection limit and selectivity using real biological samples such as blood or plasma from patients, which is the subject of future work. Since 1–3 μg/ml concentration of CRP constitutes various risk levels in patients, there is at least two orders of magnitude to work with for real samples from the current detection limit of 11 ng/ml.

Acknowledgment

JK acknowledges a Presidential Early Career Award. RKG acknowledges the financial support of the J&K Council for science and technology, Department of Higher Education, J&K, India and University Grants Commission (UGC), New-Delhi, India. This work was supported in part by NIH (R01 Ns75013).

Appendix A. Supplementary Information

Supplementary data associated with this article can be found in the online version at http://dx.doi.org/10.1016/j.bios.2014.03.027.

References

Apple, F.S., Wu, A.H., Mair, J., Ravkilde, J., Panteghini, M., Tate, J., Pagani, F., Christenson, R.H., Mockel, M., Danne, O., Jaffe, A.S., 2005. Clin. Chem. 51, 810–824.

Arumugam, P.U., Chen, H., Siddiqui, S., Jarret, A.P., Weinrich, Jejelowo, A., Li, J., Meyyappan, M., 2009. Biosens. Bioelectron. 24, 2818–2824.
Arumugam, P.U., Yu, E., Riviere, R., Meyyappan, M., 2010. Chem. Phys. Lett. 499, 241–246.
Bard, A.J., Faulkner, L.R., 2001. John Wiley and Sons Inc., New York
Brown, A.P., Anson, F.C., 1977. Anal. Chem. 49, 1589–1595.
Bryan, T., Luo, X., Bueno, P.R., Davis, J.J., 2013. Biosens. Bioelectron. 39, 94–98.
Cassell, A.M., Li, J., Nguyen-Vu, T.D.B., Koehne, J.E., Chen, H., Andrews, R., Meyyappan, M., 2009. J. Nanosci. Nanotechnol. 9, 5038–5046.
Das, J., Kelley, S.O., 2011. Anal. Chem. 83, 1167–1172.
Du Clos, T.W., 2000. Ann. Med. 32 (4), 274–278.
Hu, W.P., Hsu, H.Y., Chiou, A., Tseng, K.Y., Lin, H.Y., Chang, G.L., Chen, S.J., 2006. Biosens. Bioelectron. 21, 1631–1637.
Jacobs, C.B., Jennifer, Peairs, M.J., Venton, 2010. Anal. Chim. Acta 66, 105–127.
Kervinen, H., Palosuo, T., Manninen, V., Tenkanen, L., Vaarala, O., Manttari, M., 2001. Am. Heart J. 141, 580–585.
Koehne, J.E., Chen, H., Cassell, A., Liu, G.Y., Li, J., Meyyappan, M., 2009. Bio-Med. Mater. Eng. 19, 35–43.
Kuila, T., Bose, S., Khanra, P., Mishra, A.K., Kim, N.H., Lee, J.H., 2011. Biosens. Bioelectron. 26, 4637–4648.
Kushner, I., Sehgal, A.R., 2002. Arch. Intern. Med. 162, 867–869.
Leung, W., Chan, C.P.-Y., Leung, M., Renneberg, R., Lehmann, K., Renneberg, I., Lehmann, M., Hem-pel, A., Glatz, J.F.C., 2005. Anal. Lett. 38, 423–439.
Li, J., Koehne, J.E., Cassell, A.M., Chen, H., Ng, H.T., Ye, Q., Fan, W., Han, J., Meyyappan, M., 2005. Electroanalysis 17, 15–27.
Li, Y., Syed, L., Liu, J., Hua, D.H., Li, J., 2012. Anal. Chim. Acta 744, 45–53.
Lim, S., Yoon, S.H., Mochida, I., 2004. J. Phys. Chem. B 108, 1533–1536.
Luchansky, M.S., Washburn, A.L., McClellan, M.S., Bailey, R.C., 2011. Lab Chip 11, 2042–2044.
Martin, H.F. Meyer, Markus, Hartmann, Hans-Joachim, Krause, Gert, Blankenstein, Birgit, Mueller-Chorus, Juergen, Oster, Peter, Miethe, Michael, Keusgen, 2007. Biosens. Bioelectron. 22, 973–979.
Hennessey, H., Afara, N., Omanovic, S., Padjen, A.L., 2009. Anal. Chim. Acta 643, 45–53.
McBride, J.D., Cooper, M.A., 2008. J. Nanobiotechnol. 6 (5), 1–8.
Meyyappan, M., Sunkara, M.K., 2010. Applications in Sensors. CRC Press, Boca Raton, FL (chapter 14)
Mohammed, M.I., Desmulliez, M.P.Y., 2011. Lab chip 11, 569–595.
Nicholson, R.S., 1965. Anal. Chem. 37, 1351–1355.
Periyakaruppan, A., Arumugam, P.U., Meyyappan, M., Koehne, J.E., 2011. Biosens. Bioelectron. 28, 428–433.
Periyakaruppan, A., Gandhiraman, R.P., Meyyappan, M., Koehne, J.E., 2013. Anal. Chem. 85, 3858–3863.
Qureshi, A., Gurbuz, Y., Niazi, J.H., 2012. Sens. Actuators B: Chem. 171–172, 62–76.
Roberts, W.L., Sedrick, R., Moulton, L., Spencer, A., Rifai, N., 2000. Clin. Chem. 46, 461–468.
Siddiqui, S., Arumugam, P.U., Chen, H., Li, J., Meyyappan, M., 2010. ACS Nano 4, 955–961.
Tsai, H.Y., Hsu, C.F., Chin, I.W., Fuh, C.B., 2007. Anal. Chem. 79, 8416–8419.
Vamvakaki, V., Tsagaraki, K., Chaniotakis, N., 2006. Anal. Chem. 78, 5538–5542.
Wolf, M., Juncke,r, D., Michel, B., Hunziker, P., Delamarche, E., 2004. Biosens. Bioelectron. 19, 1193–1202.
Yang, Z., Zhou, D.M., 2006. Clin. Biochem. 39, 771–780.